Observational Evidence for Asymmetric Inertial Instability

PAUL E. CIESIELSKI, DUANE E. STEVENS AND RICHARD H. JOHNSON

Department of Atmospheric Science, Colorado State University, Fort Collins, Colorado

KELLY R. DEAN

Cooperative Institute for Research in the Atmosphere, Fort Collins, Colorado

(Manuscript received 3 March 1988, in final form 9 September 1988)

ABSTRACT

We present a detailed analysis of a mesoscale circulation phenomenon that appeared on satellite images as a group of propagating cloud wavelets. These wavelets developed on the anticyclonic side of a strong, upper-level subtropical jet in a region of negative potential vorticity (P). During their lifetime, the wavelets were located over the North American synoptic sounding network; the meteorological conditions surrounding their occurrence are examined. We investigate the various physical mechanisms that may have been responsible for generating the observed cloud wavelets. In consideration of the time scale of the wavelets and their proximity to the region where $P < 0$, inertial instability appears to be the most likely dynamical mechanism for explaining their existence. Using hourly satellite images, we determined that the wavelets propagated downstream at a phase speed 25 m s^{-1} slower than the maximum wind speed of the jet with life cycles of 4–5 h, horizontal wavelengths of ~400 km, and periods of about 1.4 h. To substantiate further our contention, the observed characteristics of the wavelets are compared to, and found to be consistent with, a theoretical model of asymmetric inertial instability.

1. Introduction

This investigation of a mesoscale circulation phenomenon was motivated by a recent study of Stevens and Ciesielski (1986; hereafter referred to as SC). In their paper they used the shallow water system of equations to investigate the preferred instabilities for horizontally sheared jet flow profiles in which the condition for inertial instability, $[\tilde{f}\bar{\eta} \leqslant 0]$, was satisfied where $\tilde{f}$ and $\bar{\eta}$ are the modified Coriolis parameter and the basic state vertical component of absolute vorticity, respectively, defined in the Appendix. Their results showed that symmetric instability—i.e., modes which display no structure in the direction of the basic state jet—is preferred only at very small vertical scales at which relatively weak dissipation could stabilize them. On the other hand, at finite but often rather small vertical wavelengths (e.g., on the order of a few kilometers for a typical midlatitude jet), asymmetric instabilities were preferred over the symmetric one. Since these unstable perturbations tend to be confined in all three space dimensions, one might expect, at least qualitatively, that results of SC could be applied to more general flows; e.g., to situations in which the mean flow varies in the vertical and jet axis directions. In view of this expectation, evidence of asymmetric inertial instability might be found in regions of negative absolute vorticity which occasionally occur on synoptic maps.

In this paper an analysis of a mesoscale circulation phenomenon is presented. Specifically, the phenomenon of interest appeared on satellite images as a group of propagating cloud wavelets located on the edge of a cirrus canopy on the anticylonic side of a strong, upper-level subtropical jet. These wavelets, which were observed between 1300 and 2200 UTC 25 February 1987, are seen most distinctly in the GOES-West infrared satellite picture at 1800 UTC (Fig. 1). *The purpose of this paper is to document that these wavelets were a manifestation of asymmetric inertial instability.* During their lifetime, the wavelets were located over the North American synoptic sounding network, affording examination of the meteorological conditions surrounding their occurrence (section 2). A particular emphasis of the analysis in section 2 is on the jet streak in which the wavelets were embedded. The characteristics of the wavelets are examined in section 3 using hourly satellite imagery. In section 4 we examine the various physical mechanisms which may have been responsible for generating the observed cloud wavelets. Of those examined, inertial instability appears to be the most likely dynamical mechanism for explaining the existence of the wavelets. To substantiate further this contention, the observed characteristics of the wavelets are compared to, and found to be consistent with, a theoretical

Corresponding author address: Mr. Paul E. Ciesielski, Dept. of Atmospheric Sciences, Colorado State University, Fort Collins, CO 80523.

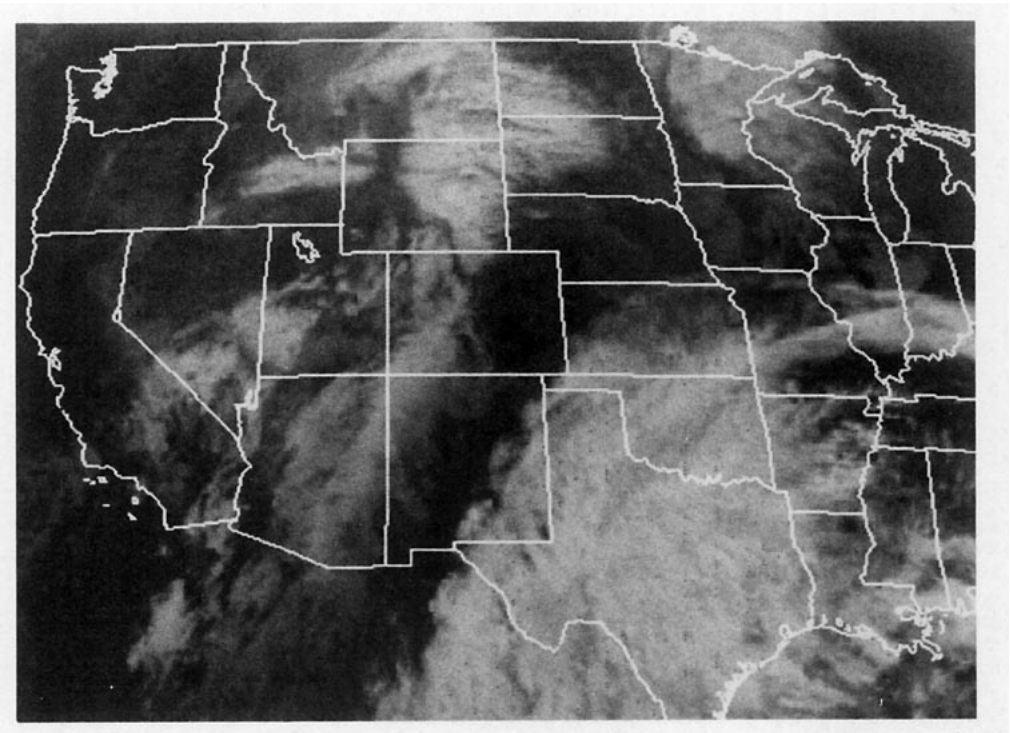

FIG. 1. The GOES-West infrared satellite image for 1800 UTC 25 February 1987 showing mesoscale cloud wavelets over New Mexico.

model of inertial instability by SC (section 5). Our conclusions are summarized in section 6.

2. Meteorological conditions

The meteorological conditions associated with the evolution of the cloud wavelets shown in Fig. 1 were investigated over the western two-thirds of the United States using conventional sounding data. Due to the paucity of these observations, only the gross features of the upper-level flow field have been captured in the analysis. This problem is compounded even further by missing data in the vicinity of the jet stream, probably due to radiosonde tracking problems.

a. Synoptic overview

On 23 February 1987, a vigorous winter storm system began affecting the western United States. By the 24th, the system was nearly occluded with an intense surface low centered over Nevada. The upper-level features were dominated by a large, positively tilted trough which extended from Saskatchewan, Canada into a cutoff low centered over Nevada. Over the next few days the system weakened, but began to reorganize and intensify over New Mexico early on the 26th as an upper-level short wave propagating through the trough moved into a position favorable for support of the surface wave.

The 1200 UTC surface weather map for 25 February (Fig. 2) displays a broad area of low pressure over the southwestern states. By 0000 UTC 26 February the surface low over southern Colorado began to deepen and move slowly south. Associated with this low was a surface cold front which extended southward from the low into southeastern Arizona. During the 25th, the southern portion of this cold front, which produced no reported precipitation on this day, moved slowly eastward with an average speed of 3.5 m s^{-1}. North of the surface low, a weak upslope condition persisted along the front range and eastern plains of Colorado and Wyoming. Precipitation amounts over this region were light (generally <0.10 in.). The only other significant precipitation amounts reported during this period occurred along the Gulf Coast (>2 in. at some locations in Texas) where moist Gulf air overran a cooler, continental air mass.

b. Analysis of the jet stream

The upper-level jet stream in which the wavelets were embedded is of particular interest to this study. Figure 3a shows the wind speed analysis at 250 mb for 1200 UTC 25 February. At this time the jet core, with maximum winds of 100 m s^{-1}, was located downstream from the confluence of polar and subtropical wind currents. Due to the sparsity of wind observations in the region of the jet core, we also present the geostrophic wind (Fig. 3b) computed from the observed height data. Although the wind analyses in Fig. 3 imply a significant ageostrophic component to the wind, particularly along the jet axis and on its anticyclonic side,

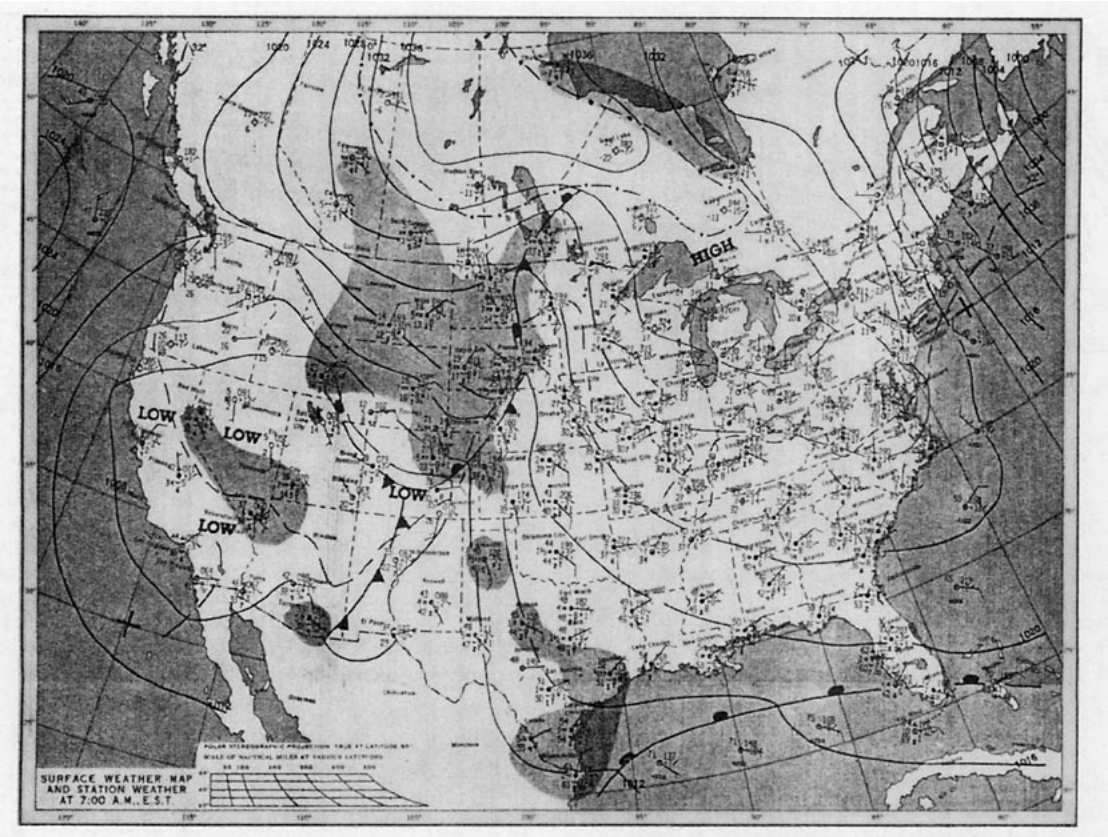

FIG. 2. National Meteorological Center (NMC) synoptic surface analysis for 1200 UTC 25 February 1987 showing position of fronts, pressure centers and isobars at 4 mb intervals.

a comparison of the magnitude of the two jets gives us confidence that the observed wind maximum of 100 m s^{-1} over data-sparse Baja is indeed realistic. (A detailed comparison of these two wind fields is given in section 4c.) The contemporaneous cross section of wind speed and potential temperature along the jet core axis (i.e., between Guaymas, Mexico and Topeka, Kansas) is shown in Fig. 4. This analysis, which was prepared from synoptic sounding data, locates the jet axis around 250 mb; below this level, vertical shears of 40 m s^{-1} (100 mb)$^{-1}$ were present. South of the jet axis, horizontal shears were 10 m s^{-1} (100 km)$^{-1}$. It is in this region of strong anticyclonic shear that the cloud wavelets were observed.

In the 12 h period following 1200 UTC 25 February, the structure of the jet stream underwent several significant changes. (Figures 5 and 6 show the 250 mb isotach analysis and the along-jet axis cross section for 0000 UTC 26 February, respectively.) First, in conjunction with a deepening trough over the western United States, the jet stream axis developed a more meridional orientation. Second, from its position over Baja California on the twenty-fifth, the core of maximum winds moved at an average speed of ~45 m s^{-1} to a position over the central United States. Although the maximum intensity of the jet remained approximately constant (~105 m s^{-1}), the horizontal wind shear on the anticyclonic side of the jet core reduced about 30% to 7 m s^{-1} (100 km)$^{-1}$. Finally, the altitude of the jet core (as determined from synoptic sounding data) rose slightly such that on the twenty-sixth, maximum winds at stations DDC and 3NO were at 200 mb. This behavior suggests a tendency for the jet streak to remain on a constant isentropic surface since the cross section on the twenty-fifth shows upward sloping isentropes along the axis of the jet.

3. Characteristics of the cloud wavelets

Figure 7 shows a series of nine consecutive, hourly, infrared (IR) satellite images from 1300 to 2100 UTC 25 February. These images, which were taken by the GOES-West satellite, have a horizontal resolution of 4 km at satellite subpoint. Most of the features seen in these pictures are also obvious in the corresponding visible images; however, the clouds were not well illuminated in the visible images until 1600 UTC. The predominant large-scale features in these satellite images are the cloudiness associated with the surface low over New Mexico and the broad shield of mainly high-

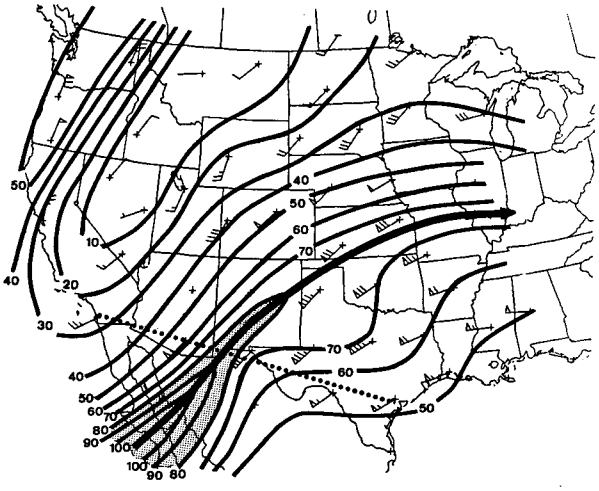

FIG. 3a. The 250 mb wind speed analysis (m s^{-1}) at interval of 10 m s^{-1} for 1200 UTC 25 February 1987. Wind reports are from synoptic sounding network. Location of sounding stations is indicated by plus sign (+); this symbol plotted without associated wind barb indicates that the wind data was missing. The jet stream axis is shown with a heavy solid arrow and wind speeds greater that 80 m s^{-1} are stippled. Dotted line shows projection for cross sections in Figs. 13 and 16.

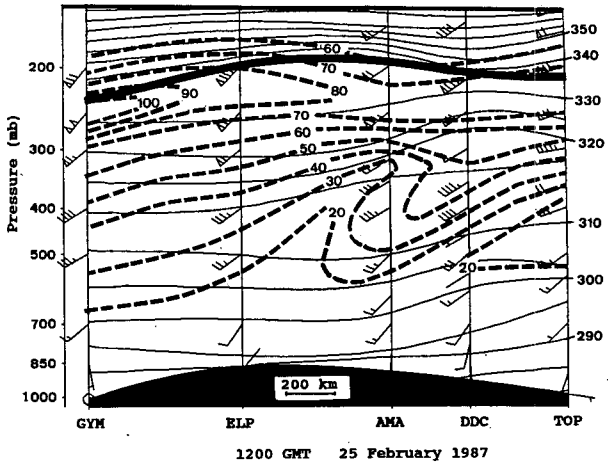

FIG. 4. Cross sectional analysis of wind speed (m s^{-1}, heavy dashed lines) at intervals of 10 m s^{-1} and potential temperature (K, thin solid lines) at intervals of 5 K along the jet core axis for 1200 UTC 25 February 1987. Tropopause represented with heavy solid line. Rawinsonde soundings are from Guaymas, Mexico (GYM), El Paso, Texas (ELP), Amarillo, Texas (AMA), Dodge City, Kansas (DDC), and Topeka, Kansas (TOP).

level clouds extending from southwest of Mexico to over the central states. This latter feature, which is often referred to as a "baroclinic cloud leaf," is associated with a rising, moist airstream within the subtropical jet. Weldon (1979) has noted that the sharp western boundary of the upper tropospheric cloud leaf often coincides closely with a wind speed maximum or with a zone of strong winds. In the course of the pictorial sequence in Fig. 7, the cloud leaf is observed to expand gradually northward and westward in response to horizontal displacements of the jet axis core.

The images prior to the sequence in Fig. 7, show the poleward edge of the cloud leaf to be relatively sharp and unperturbed. An excellent discussion of the factors which cause the sharp edge along the poleward boundary of the jet stream cirrus is given by Durran and Daniel (1988). At 1300 UTC one can see the first evidence that the cloud leaf over Baja, California was being perturbed. During the next 3 h two distinct wavelets grew over this region and propagated northeastward parallel to the jet core axis until they appear to dissipate around 1700 UTC. Simultaneously with the dissipation of these wavelets, a second group began

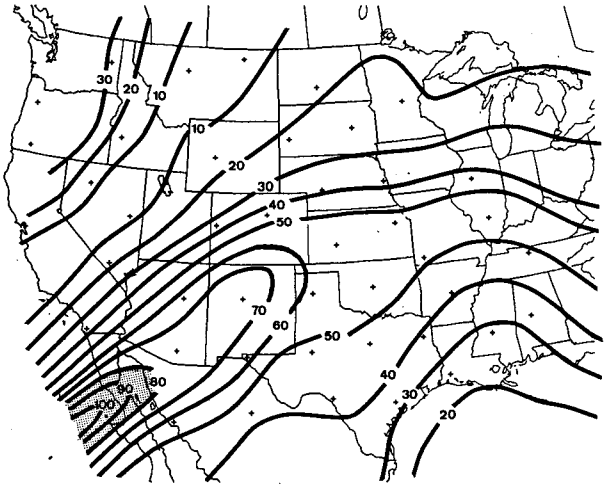

FIG. 3b. The 250 mb geostrophic wind speed analysis (m s^{-1}) at intervals of 10 m s^{-1} for 1200 UTC 25 February 1987. Winds were computed from geopotential height data from synoptic sounding network. Location of sounding stations is indicated by plus. Wind speeds greater than 80 m s^{-1} are stippled.

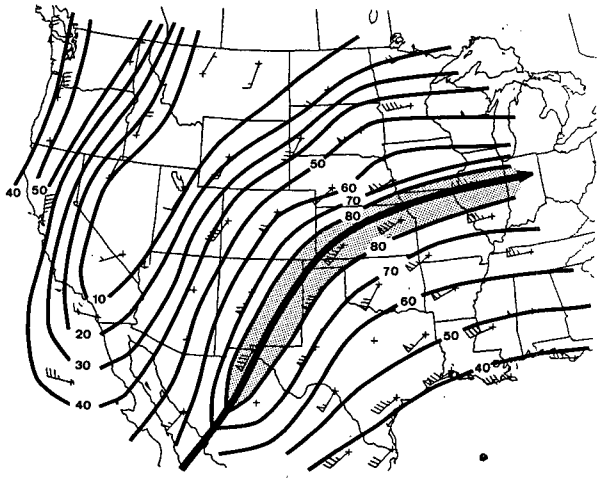

FIG. 5. As in Fig. 3a, but for 0000 UTC 26 February 1987.

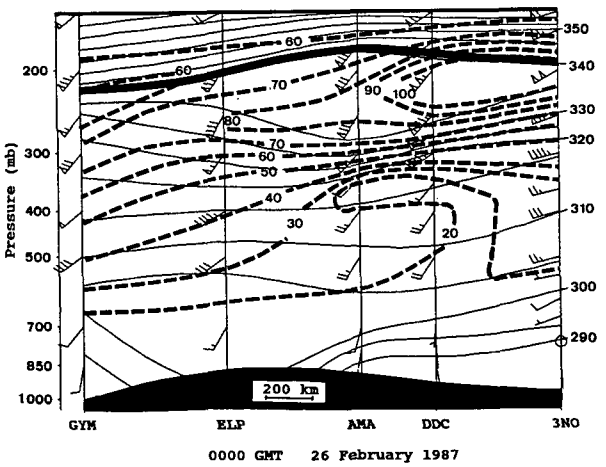

FIG. 6. Cross sectional analysis of wind speed (m s^{-1}, heavy dashed lines) at intervals of 10 m s^{-1} and potential temperature (K, thin solid lines) at intervals of 5 K along the jet core axis for 0000 UTC 26 February 1987. Tropopause represented with heavy solid line. Rawinsonde soundings are from Guaymas, Mexico (GYM), El Paso, Texas (ELP), Amarillo, Texas (AMA), Dodge City, Kansas (DDC), and Omaha, Nebraska (3NO).

to form near the United States–Mexican border. By 1800 UTC three cloud wavelets are observed. These wavelets propagated in a similar fashion to those described above and can be tracked until they dissipated around 2200 UTC; no wavelets could be identified after this time.

By creating a loop of the satellite images in Fig. 7, we were able to track the position of individual wavelets from 1 h to the next. Figure 8 shows the hourly positions of one of these wavelets superimposed with the locations of the jet axis from Figs. 3a and 5. Figure 8 also depicts the orientation and size of the wavelet during its life cycle. The general shape of the wavelets was that of an ellipse with its major axis oriented parallel to the jet axis. The life cycle of these wavelets appeared to have a growth stage (~1 h), a mature stage (2–3 h) and a decay stage (~1 h) in which their identification becomes increasingly difficult. During their mature stage the wavelets varied in size from 200–250 km (along their major axis) and 65–100 km (along their minor axis). From Figs. 7 and 8 it appears that the wavelets moved parallel to the jet axis, in groups of two or three, and at a distance about 50 km to its anticyclonic side. In their mature stage the average distance between the centers of adjacent wavelets was ~400 km. Using this scale as the wavelength (L_x) of the wavelets, and noting that their average speed of propagation (c) was ~80 m s^{-1}, we arrive at a period (L_x/c) for the wavelets of 1.4 h.

To estimate the vertical level of the wavelets, the individual point (pixel) values of the satellite images were first converted into radiances and then into brightness or equivalent blackbody temperatures (T_B). The resolution using this technique is approximately 1.5°C at typical cloud top temperatures. Due to the wavelength at which the infrared images are sensed (the window region of 10.5–12.6 μ), the clear atmosphere is nearly transparent and T_B measures the radiative temperature of the cloud, the surface, or combinations of the two within the 4 km square field (Minnis and Harrison 1984). In the case of thin cirrus clouds, some of the radiative energy from the warm surface below passes through them resulting in a relatively higher T_B than a thick cirrus canopy at the same level. This appears to be the case near the edges of the cloud leaf and in the wavelets (Fig. 7) where the analyzed T_B was nearly 5°C warmer than in the interior of the cloud canopy where the T_B ranged from −44° to −52°C. Based on these values and the observed temperatures from a representative sounding (Amarillo, Texas at 0000 UTC 26 February, Fig. 9), it appears that the wavelets and cloud leaf were composed of ice particles with cloud tops around 250 mb. In addition, the moist layer centered around 280 mb in the Amarillo sounding suggests that these cirrus clouds were limited in their vertical extent to a layer about 50 mb (~1.5 km) deep. Although the wavelets were an effective tracer in the layer of cirrus clouds, they offer us no means of estimating the vertical depth of the perturbed flow.

4. Dynamical mechanism for perturbed flow

In this section we examine three types of dynamical mechanisms (gravity waves, barotropic instability, and inertial instability) to ascertain which is the most likely cause for the perturbed flow described above. At the low temperature in which the wavelets existed, instabilities associated with phase changes can be ruled out.

a. Gravity waves

Gravity waves, which are fluid motions in which gravity provides the restoring force, occur over a broad spectrum of temporal and spatial scales. Although gravity waves are generated by a multitude of sources (Stevens and Crum 1987), we consider here the most probable ones with consideration to our problem: convection, geostrophic adjustment, vertical shear, and flow over mountains.

Previous studies (Raymond 1975; Lindzen 1974a) have documented that latent heat released in strong convection is capable of efficiently forcing gravity waves. In other cases where convective forcing is weaker, the existence of gravity waves requires a duct from which little wave energy can escape (Lindzen and Tung 1976). In both cases the gravity waves are observed to move in a direction roughly along the mean flow. However, in the case under consideration, both the region of strong convection (over the Gulf Coast) and weak convection (over Colorado and Wyoming) were well downstream (more than 1500 km) from where the wavelets were first observed over Baja, Cal-

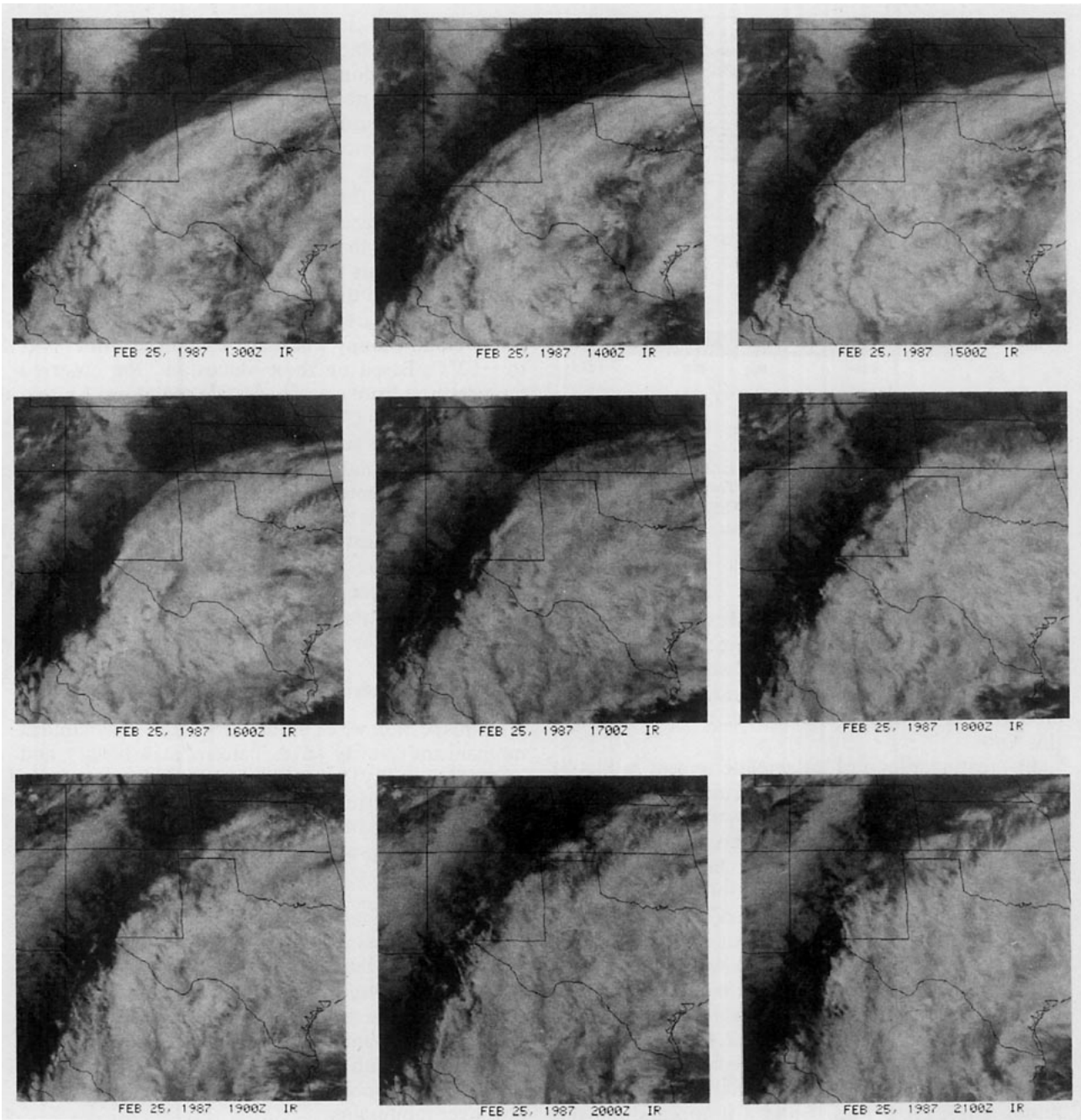

FIG. 7. Hourly GOES-West infrared satellite images from 1300–2100 UTC 25 February 1987 showing life cycle of mesoscale cloud wavelets.

ifornia. Thus, it is highly improbable that the observed wavelets were gravity waves forced by convection.

Since Fig. 3 implied a significant ageostrophic component to the flow in the region of the jet, we now consider geostrophic adjustment as a possible source mechanism for the wavelets. In the absence of geostrophic balance, energy propagation by small-scale gravity waves will act to restore geostrophy after a period of adjustment (Arakawa and Lamb 1977). The propagation of energy, and thus the gravity waves fronts, will be directed away from the area of imbalance which in our case is largest in the vicinity of the jet core. Possible evidence for this adjustment process can be seen with a color enhanced loop of the IR images in Fig. 7. In this manner elongated undulations in the cloud top temperature are observed propagating through the cirrus canopy. These undulations are oriented parallel to the jet axis and appear to emanate from it as in a geostrophic adjustment process. In contrast, the wavelets are spatially fixed relative to the core

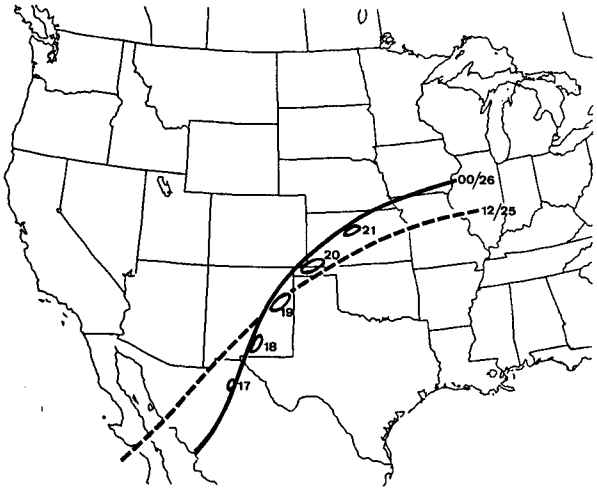

FIG. 8. Hourly positions and shape of a single cloud wavelet inferred from satellite images in Fig. 7. Numbers plotted by wavelet indicate the time (UTC) at which that position was observed. Also shown here are the positions of the jet stream axis at 1200 UTC 25 February 1987 (dashed line) and at 0000 UTC 26 February 1987 (solid line).

of strongest winds, and thus do not remove momentum and energy from the jet region.

As noted in the earlier jet stream analysis, vertical shears of 40 m s^{-1} (100 mb)$^{-1}$ were observed below the level of the jet axis. In shear zones such as this, clear air turbulence is often observed and attributed to Kelvin–Helmholz (KH) instability (Drazin and Howard 1966) and/or neutral propagating internal gravity waves (Hines 1960). The condition for the existence of KH instability (Howard 1961) and neutral wave solutions (Booker and Bretherton 1967) is given in terms of the Richardson number (Ri) as

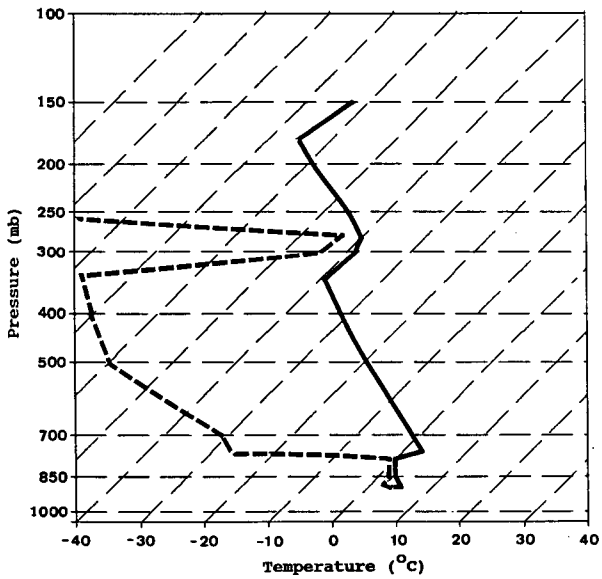

FIG. 9. Skew $T/\log P$ plot of 0000 UTC 26 February 1987, Amarillo, Texas upper-air sounding.

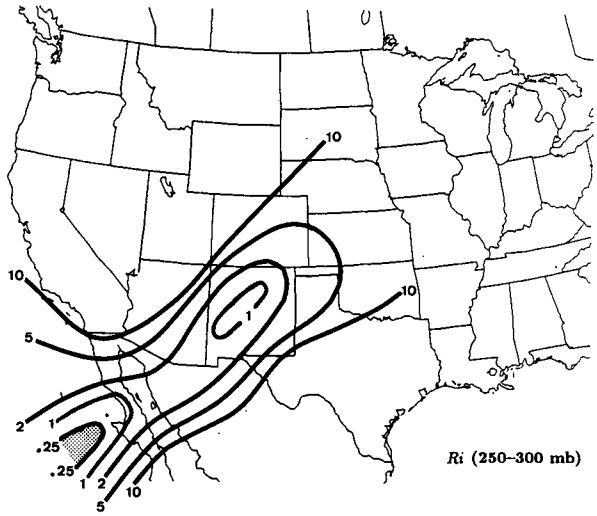

FIG. 10. Analysis of Richardson number (Ri) at 1200 UTC, 25 February 1987 for the layer 250–300 mb. Areas with Ri < ¼ are stippled.

$$\mathrm{Ri} = N^2 \Big/ \left(\frac{dU_0}{dz}\right)^2 < \frac{1}{4}, \qquad (1)$$

where N is the Brunt–Väisälä frequency,

$$\left[\frac{g}{\theta}\left(\frac{d\theta}{dz}\right)\right]^{1/2},$$

and the denominator of (1) is the vertical shear squared.

To determine if the condition, Ri < ¼, was satisfied in our present case, we evaluated Ri at 1200 UTC 25 February for three layers between 200 and 400 mb. Since the directional shear with height was small within this layer, we evaluated the denominator in (1) by taking the difference in the magnitude of the geostrophic wind between two levels. Figure 10 shows an analysis of Ri in the layer where this field attained its smallest values. This figure shows that the condition given by (1) is satisfied off the coast of Baja. In addition, a narrow minimum of Ri lies along and below the jet axis coincident with the large vertical shear in this region.

Since the condition for the existence of KH instability and/or neutral gravity waves is satisfied in our present case, we consider here what their characteristics might be. In Lindzen (1974b), observed disturbances in vertical shear zones and theoretical estimates of KH instability and internal gravity waves were shown to have lifetimes and horizontal scales on the order of 10 min and 10 km, respectively. Since these temporal and spatial characteristics are considerably different from those of the observed cloud wavelets (4–5 h and 400 km), we can eliminate these mechanisms which result from vertical shear as the source of the wavelets. It is worth noting however, that inspection of a high resolution (2 km) visible image at 1800 UTC on the twenty-

fifth reveals waves in the cloud field over southwestern New Mexico with characteristics and scales typical of KH instability.

Within this same class of instabilities, Jones (1968) investigated the reflection of gravity waves at a critical level; that is, where their Doppler-shifted frequency was zero. His results showed that when Ri < ¼ at a critical level, overreflection could occur whereby the amplitude of the reflected wave exceeded that of the incoming wave. Since the conditions for overreflection are present in our case, one might expect such a mechanism to generate waves with scales and amplitudes somewhat larger than classical KH instabilities but still not on the order of the observed wavelets.

Under statically stable conditions, air parcels which are forced to flow over a mountain will undergo buoyancy oscillations as they move downstream from the barrier. These gravity wave motions can generate wave clouds if the associated vertical motion and moisture are sufficient enough. An excellent summary on the dynamics of lee mountain waves is given by Smith (1979). Since the trajectory of the jet stream in the present analysis was over the mountainous terrain of Mexico, one might hypothesize that the observed wavelets were a manifestation of lee mountain waves. Although these mountains may have had an influence on the structure of the cloud wavelets observed after 1700 UTC, the wavelets were first observed at 1300 UTC directly over Baja which is a few hundred kilometers upstream of any significant mountains.

b. Barotropic instability

The necessary condition for barotropic instability due to horizontal shear is that the gradient of absolute vorticity of the mean current must vanish somewhere in the fluid (Kuo 1949). This condition was satisfied at 1200 UTC 25 February on the anticyclonic side of the jet where the absolute vorticity is at a minimum. Although the condition for barotropic instability was met in this situation, the results of SC show that the growth rates for this type of instability are slow relative to inertial instability. Stevens and Ciesielski (1986) estimated the maximum growth rate for asymmetric inertial/shear instability to be $\frac{2}{3}\epsilon$ and the maximum growth rate of barotropic instability to be $\frac{1}{10}\epsilon$, where $\epsilon \equiv (-\bar{\eta}\hat{f})^{1/2}_{\max}$ is the maximum nondimensional growth rate for symmetric, infinitesimal inertial instability.

These theoretical estimates of growth rate are now applied to our present study: to the south of the jet maximum at 1200 UTC on the twenty-fifth, $\hat{\epsilon} = 0.53$. (The estimated parameter, $\hat{\epsilon}$, is defined in the Appendix which considers how theoretical work of SC should be regarded to facilitate a comparison between it and observations.) This value of $\hat{\epsilon}$ represents an unstable *e*-folding time scale, $\tau = (2\Omega\hat{\epsilon})^{-1}$, equal to 3.6 h for symmetric, infinitesimal inertial instability; 5.4 h (or $\frac{3}{2}\tau$) for asymmetric inertial instability; and 36.2 hours (or 10τ) for barotropic instability. Thus, it would seem more reasonable that the observed wavelets, which grew and decayed in a time frame of 4–5 h, were a manifestation of inertial instability.

c. Inertial instability

In the general case of flow with horizontal and vertical shear, potential vorticity (P) replaces absolute vorticity ($\bar{\eta}$) in determining the inertial instability criterion (Hoskins 1974; Stevens 1983). A necessary condition for inertial instability is $fP < 0$ somewhere in the fluid, where P, as first derived by Ertel (1942), is given by

$$P = \frac{1}{\rho}(\zeta_a \cdot \nabla\theta). \tag{2}$$

In this equation, ζ_a is the absolute, three-dimensional vector vorticity, ρ the density and θ the potential temperature. Using the hydrostatic approximation, this definition may be rewritten as

$$P = -g\left\{\underbrace{-\frac{\partial v}{\partial p}\left(\frac{\partial\theta}{\partial x}\right)_p + \frac{\partial u}{\partial p}\left(\frac{\partial\theta}{\partial y}\right)_p}_{\text{PV}} + \underbrace{\left[\left(\frac{\partial v}{\partial x}\right)_p - \left(\frac{\partial u}{\partial y}\right)_p + f\right]\frac{\partial\theta}{\partial p}}_{\text{PH}}\right\}, \tag{3}$$

where g is the gravitational acceleration, p pressure, and u and v are the velocity components in the eastward and northward directions, respectively. The subscript p denotes that derivatives are taken on constant pressure surfaces. Equation (3) shows that P has contributions due to the both horizontal (PH) and vertical (PV) shear.

Analysis of potential vorticity using (3) requires the construction of an isobaric dataset consisting of grid point values of potential temperature and wind on a set of specified pressure levels. Due to the large number of missing and bad wind observations in the vicinity of the jet, particularly above 250 mb, we elected to use geostrophic wind in the evaluation of P. Height data, which is used in the computation of geostrophic wind, had much better spatial coverage than winds for the times and levels under consideration. For comparison sake, an analysis of P computed with observed winds will be presented.

Two major discrepancies are worth noting between the wind fields in Fig. 3a, b. The first of these is over the region of Baja where the axis of maximum geostrophic winds is displaced nearly 200 km farther north than the observed jet streak. Shapiro (1981) noted that the ageostrophic component of the wind can be large in the vicinity of jet streaks. The second major discrepancy between the two wind analyses is observed

along the western side of the upper-level ridge where parcel trajectories are predominately anticyclonic. Over this region the geostrophic approximation, which neglects the effect of centripetal acceleration due to the curvature of the flow, underestimates the magnitude of the observed wind; this is especially obvious over the Gulf of Mexico where the differences are nearly a factor of 2. By assuming gradient wind balance, which includes the effects of centripetal acceleration, and a reasonable radius of curvature ($\approx$2000 km), the computed wind speeds over the Gulf increase nearly 50%. In spite of this improvement, we chose to use geostrophic winds in the computation of P, since over the region where the instabilities were observed, there is little difference between gradient and geostrophic winds. Secondly, where centripetal accelerations are significant, estimating the radius of curvature of air parcel trajectories is highly subjective.

The grid point data needed for the computation of P was constructed at 200, 250, 300, and 400 mb by performing a Barnes objective analysis (Barnes 1973) on the station data. We limited our analyses to these levels since the wavelets, as described above, were confined to the 250–300 mb layer; above 200 mb, the data were insufficient to perform any type of meaningful analysis. Using the gridded data, potential vorticity fields were computed for three layers (200–250 mb, 250–300 mb, and 300–400 mb). Derivatives in (3) along a pressure surface were computed using centered finite differences; these values were then averaged over adjacent levels to obtain layer averages. Derivatives with respect to pressure in (3) were computed by taking differences between adjacent levels.

Using the procedure outlined above, Fig. 11 shows the analysis of potential vorticity for three layers between 200 and 400 mb at 1200 UTC on the twenty-fifth. At this time, an elongated maximum in P extending from western Montana into southern California reflects the position and orientation of the upper-level trough. In addition, the maximum in P increased with height, implying an increase in the intensity of the circulation up to the level of the jet core. The key feature in the analysis of potential vorticity on the twenty-fifth is a region of negative potential vorticity over New Mexico extending southwestward to over Baja. This region of negative P is evident in all three layers but is most pronounced above 300 mb where the anticyclonic shear associated with the jet streak was strongest. Due to the discrepancy noted earlier between the observed and geostrophic wind analyses over Baja, the region of negative P over this area probably existed farther south than Fig. 11 indicates. This assertion is further substantiated by the potential vorticity analysis computed using observed winds (Fig. 12) which places the region of negative P in a more southerly location than Fig. 11. Also shown in Fig. 12 are the contributions to P due to PH and PV. These analyses show that the contribution due to PH is generally one–two orders of magnitude larger than that due to PV. However, in the region where the wavelets were observed, the combination of strong vertical shear and weak horizontal shear made their contributions comparable.

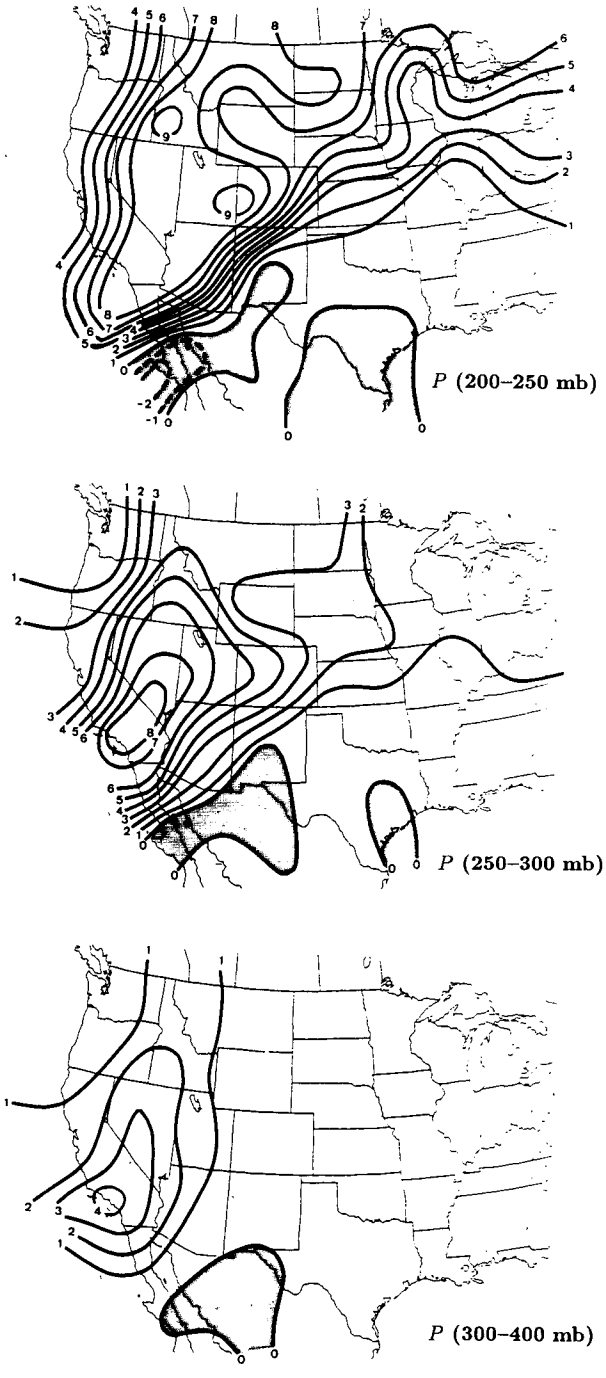

FIG. 11. Analysis of potential vorticity (m^2 K kg^{-1} s^{-1}) computed using geostrophic winds at 1200 UTC 25 February 1987 for the layers 200–250 mb (top panel), 250–300 mb (middle panel) and 300–400 mb (bottom panel). Values in figure have been multiplied by 10^6. Areas of negative potential vorticity are shaded.

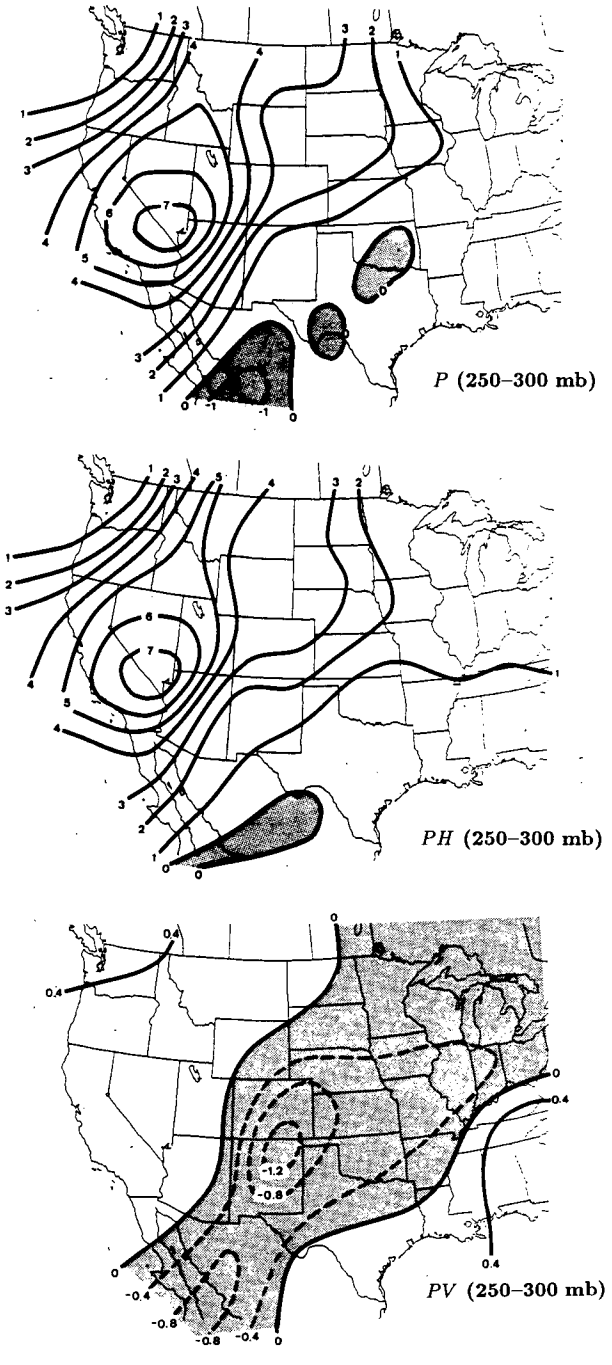

FIG. 12. Analyses of potential vorticity (m^2 K kg^{-1} s^{-1}) computed using observed winds at 1200 UTC 25 February 1987 for the layer 250–300 mb (P, top panel), and contributions to P due to horizontal (PH, middle panel) and vertical shear (PV, bottom panel). Values in figure have been multiplied by 10^6. Areas of negative potential vorticity are shaded.

An alternative view of the potential vorticity analyses is presented in Fig. 13, which shows its relationship to the geostrophic wind in a cross section through the jet. At the time of this analysis, the core of the jet streak and the associated region of large negative P were located several hundred kilometers upstream of where this cross section was taken. The X in Fig. 13 shows the observed location of the wavelets at 1800 UTC. From the analyses presented in Figs. 11–13, we conclude that *the condition for inertial instability was satisfied in the region and over the time frame that the wavelets existed.* A second area of weak negative potential vorticity is evident over southeastern Texas; however, its existence is questionable due to our lack of confidence in the geostrophic winds over this area.

The potential vorticity analysis at 0000 UTC on the twenty-sixth (Fig. 14) shows little change from the general pattern 12 h earlier (Fig. 11); the large maximum in P was still located over the western states in conjunction with the deep upper-level trough and the area of weakly negative P still remained over Texas. The only significant change was that the area of negative P directly to the anticyclonic side of the jet streak, which on the twenty-sixth was positioned over Kansas, no longer existed. This suggests that the mechanism responsible for generating the wavelets also resulted in the elimination of the region of negative P.

It is instructive here to consider how the region of negative P in Figs. 11–13 may have been generated. Air parcels conserve their potential vorticity as they move about in the absence of frictional and diabatic

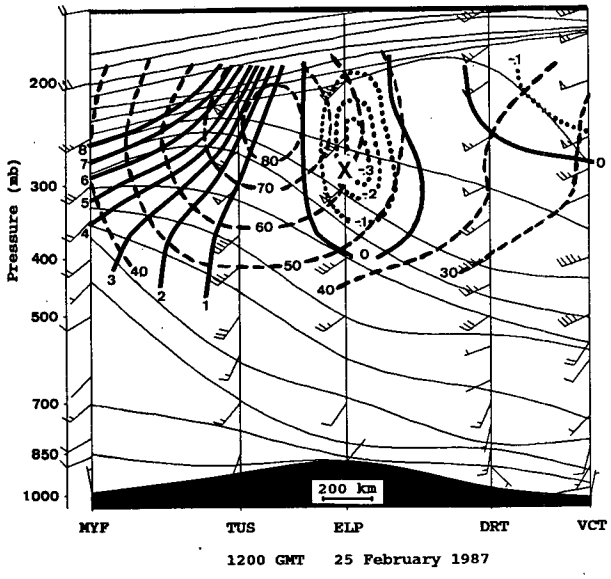

FIG. 13. Cross sectional analysis of geostrophic wind speed (m s^{-1}, heavy dashed lines) at intervals of 10 m s^{-1} and potential temperature (K, thin solid lines) at intervals of 5 K along dotted line in Fig. 3a for 1200 UTC 25 February 1987. Plotted wind barbs show observed wind (m s^{-1}) for comparison to geostrophic wind speed. Analysis of potential vorticity (m^2 K kg^{-1} s^{-1}) computed using geostrophic winds; heavy solid lines for positive values at intervals of 10^{-6} and dotted lines for negative values at intervals of 10^{-7}. Position of wavelets at 1800 UTC on the twenty-fifth are denoted with an X. Rawinsonde soundings are from San Diego, California (MYF), Tucson, Arizona (TUS), El Paso, Texas (ELP), Del Rio, Texas (DRT), Victoria, Texas (VCT).

effects. Neglecting frictional effects, the potential vorticity equation can be written as

$$\frac{dP}{dt} = \frac{1}{\rho}(\zeta_a \cdot \nabla Q), \tag{4}$$

where Q represents diabatic heating. If we rotate the x-axis (as in the Appendix) so that it is aligned with the observed jet axis and neglect horizontal gradients of vertical motion, (4) can be rewritten using the hydrostatic approximation as

$$\frac{dP}{dt} = -g\left[\eta\left(\frac{\partial Q}{\partial p}\right) + \frac{\partial u}{\partial p}\left(\frac{\partial Q}{\partial y}\right)_p\right]. \tag{5}$$

To evaluate the effects of Q on the potential vorticity, we assume a simple profile for Q in the cirrus cloud layer (Fig. 15). The depth of the cloud layer in this profile (50 mb or 1.5 km) was surmised from the Amarillo sounding (Fig. 9); the magnitude of the diabatic heating in the cloudy layer (5 K day^{-1}) accounts for infrared radiational effects and is typical of heating rates in thin ($\sim$1 km) cirrus canopies with no underlying clouds (cf. Fig. 11 from Ackerman et al. 1988). Although this heating magnitude is only a first-order estimate [e.g., Starr and Cox (1985) showed that the effects of condensation heating could be significant during the initial stages of cirrus cloud formation], the argument which follows depends crucially upon the sign of Q in the cirrus cloud layer rather than its absolute magnitude. From the heating profile in Fig. 15, we estimate the vertical and horizontal gradients of Q in (5) as ($\pm$5 K day^{-1}/25 mb) and ($-$5 K day^{-1}/20 km), respectively. One should note that $\partial Q/\partial y$ is large only along the edge of the cirrus shield.

Using this information in conjunction with observed values of η ($\approx 10^{-5}$ s^{-1}) and $\partial u/\partial p$ (-20 m s^{-1}/50 mb) in the vicinity of the wavelets, we find that the second term on the right-hand side of (5) is an order of magnitude larger than the first term, resulting in a rate of change in P of -4.3×10^{-7} m^2 K kg^{-1} s^{-1} per hour. To put rate of change in perspective, if the above assumptions are valid over a period of 3 h along the trajectory of an air parcel, the potential vorticity of a parcel with an initial value of 1.0×10^{-6} m^2 K kg^{-1} s^{-1} would decrease to -3.0×10^{-7} m^2 K kg^{-1} s^{-1}, which is the value of P in Fig. 13 where the instability was observed. Thus, where the diabatic effects along a cirrus shield boundary couple with strong vertical shear, a mechanism exists with the potential for generating areas of negative P. It is worth noting that the region of the atmosphere over which this mechanism is confined coincides with the location of the observed instability.

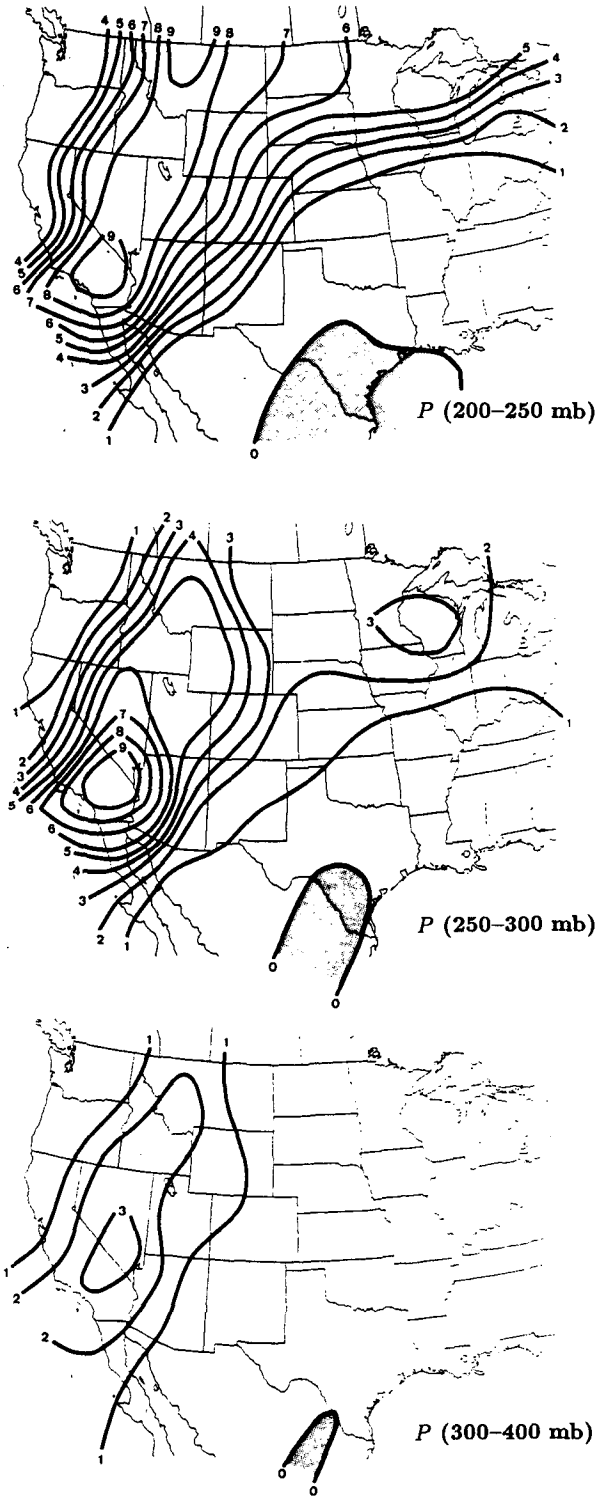

FIG. 14. As in Fig. 11, except for 0000 UTC 26 February 1987.

5. Comparison of observation with theory

Since inertial instability appears to be a reasonable explanation for the appearance of the wavelets, we now compare their characteristics (as discussed in section 3) with theoretical estimates for asymmetric inertial instability from SC. One might reasonably question

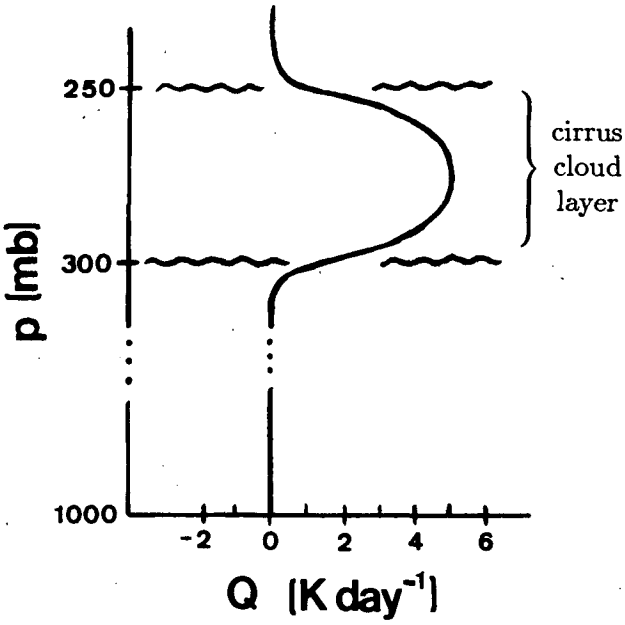

FIG. 15. Idealized diabatic heating profile which accounts for infrared radiational effects within a cirrus cloud layer.

the applicability of SC's results, which were obtained for a barotropic basic state, to this study where the wavelets are embedded in a baroclinic flow. However, as stated in the Introduction, SC found that asymmetric instabilities are preferred over symmetric ones even at small vertical scales, which suggests that their results could be applied, at least qualitatively, to more general flows with vertical shear. Secondly, SC's results are the only ones we are aware of that deal with asymmetric modes as a manifestation of inertial instability. Further justification for using SC's results as a theoretical basis for the observed wavelets is given in the Appendix.

For a Bickley jet of 75 m s^{-1} and a half-width of 3° at latitude 45°N, SC found that asymmetric perturbations would propagate at ~45 m s^{-1} with respect to the ground (or 30 m s^{-1} slower than the maximum wind). The observed wavelets propagated at an average speed of 80 m s^{-1} (or 25 m s^{-1} slower than the maximum wind). As mentioned earlier, SC estimated that asymmetric perturbations would have a maximum growth rate bound of $\frac{2}{3}\epsilon$, which for the observed jet corresponds to an unstable e-folding time scale of 5.4 h; the wavelets life cycle was between 4–5 h. Finally, SC estimated that the length scale of the asymmetric perturbations in the direction of the jet axis ($L_x/2\pi$) is comparable to the width of the unstable region. For the observed wavelets this length scale is ~70 km, whereas the width of the region with $P < 0$ varied between 100–200 km in the 250–300 mb layer. Table 1 summarizes these comparisons. Although we have no means of estimating the vertical depth of the perturbed flow from the observed data, SC found that asymmetric modes of instability are preferred over the symmetric one for vertical wavelengths greater than 3 km.

We must qualify the theoretical estimates in Table 1 which are computed from the fields of potential and absolute vorticity. Since the fine-scale features of the flow cannot be resolved due to the sparseness of the sounding data, the observed jet maximum and associated gradients are smoothed in the analysis. Such filtering in turn affects the computation of derived fields; in particular, areas of negative potential and absolute vorticity are most likely overestimated in size and underestimated in magnitude. In consideration of these effects, the theoretical estimates in Table 1 are presented merely as upper bounds on the "true" values. Despite the data deficiencies and simplifications inherent in the theoretical estimates (cf., SC for details), *the agreement found in the above comparisons lends significant credence to our hypothesis that the observed wavelets were a manifestation of asymmetric inertial instability.*

Since the theoretical results of SC were derived by assuming dry, barotropic dynamics, it is instructive to consider our present case within the context of Emanuel's (1983a) work which takes into account the effects of moisture and vertical shear. Using Emanuel's analysis techniques, we assess the stability of the moist baroclinic flow depicted in the cross section of Fig. 13 to finite, slantwise, reversible displacements. This was done by constructing a second cross section of equivalent potential temperature (θ_e) and pseudoangular momentum (M) in the plane orthogonal to the mean shear (Fig. 16). The quantity M defined here as, $v_g + fx$, was calculated from the horizontal distance from San Diego in the plane of the cross section (x) and the component of the geostrophic wind from 200° (v_g).

Above El Paso near 250 mb the westward deflection of the M surfaces in Fig. 16 reflects the presence of a strong jet in this region of the domain. If the flow were barotropic (i.e., no vertical shear), then the M surfaces would vary in x alone. Above Victoria, Texas, the analysis indicates that the lower troposphere is conditionally unstable to slantwise, as well as vertical displacements. In the region where the wavelets occurred, denoted by an X in the cross section, a patch of near-neutrality extends from there eastward and downward to about 400 mb. According to Emanuel's criterion, parcels in this region are neutral to moist, slantwise displacements. However, upstream of this cross section

TABLE 1. Comparison of theoretical estimates for asymmetric inertial instability based on Stevens and Ciesielski's (1986) results with observed characteristics of cloud wavelets.

Characteristics of instability	Theoretical	Observed
Phase speed relative to maximum wind	−30 m s^{-1}	−25 m s^{-1}
Time scale	≤5.4 h	4–5 h
Horizontal length scale	≤100–200 km	70 km
Period	≤2–4 h	1.4 h

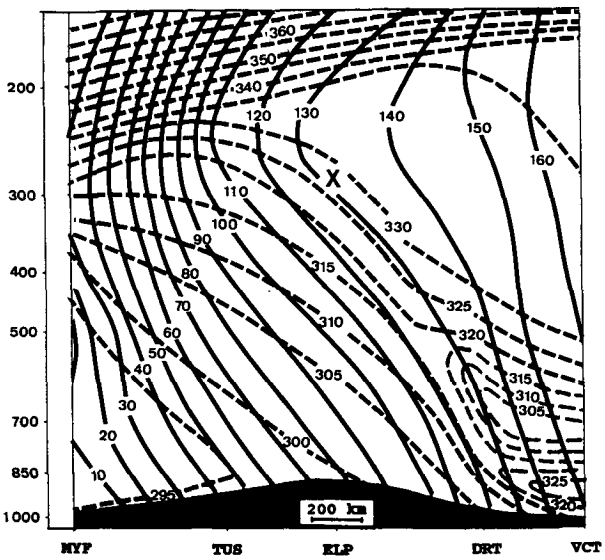

FIG. 16. Cross sectional analysis from San Diego, California (MYF), to Victoria, Texas (VCT) at 1200 UTC 25 February 1987. Solid lines denote M (m s^{-1}) at intervals of 10 m s^{-1}; dashed lines are θ_e (K) at intervals of 5 K. Position of wavelets at 1800 UTC on the twenty-fifth are denoted with an X.

where vertical shears are stronger, M surfaces below the jet core would have even steeper slopes than shown in Fig. 16; thus parcels in this region would likely be unstable to moist, slantwise displacements. With this configuration, Emanuel asserts that the resulting motion would manifest itself as symmetric instability, as opposed to asymmetric instability which was observed in our present study. Nevertheless, the analysis shown in Fig. 16 suggests that vertical shear and moisture played important roles in the dynamics of the observed wavelets.

6. Concluding remarks

From the foregoing analyses, we hypothesize the following scenario of events. At 1200 UTC on the twenty-fifth, a strong jet streak embedded within the subtropical jet current was observed over Baja. Directly to the right of this jet streak, there existed an area of negative potential vorticity associated with the strong anticyclonic shear in this region. During the next 12 h this jet streak moved along the front side of a deep upper-level trough over the western United States at an average speed of ~45 m s^{-1}. During this period asymmetric inertial instability developed in response to the negative potential vorticity. This instability was manifested in a series of mesoscale cloud wavelets which formed along the western edge of a cirrus canopy. These wavelets, which were observed in satellite images between 1300 and 2200 UTC on the twenty-fifth, propagated parallel to the jet core at an average speed of 80 m s^{-1}. These unstable perturbations acted to mix the flow, thereby reducing the horizontal shears until the region of negative potential vorticity was eliminated.

Assuming that the first evidence of the instability at 1300 UTC on the twenty-fifth was, in fact, near the time of its onset, it becomes necessary to explain why a region of negative P should exist for some time and then suddenly realize its instability. It has been suggested (Emanuel, personal communication) that condensation of water vapor, however small its effect in the vicinity of the wavelets, might serve to push the flow over the brink of instability. One must realize however, that prior to 1200 UTC on the twenty-fifth, the jet core, which the wavelets appeared spatially fixed to, was south of 23°N (i.e., the southern extent of our satellite dataset). Thus, it is not possible to determine whether instability was present before 1200 UTC and how long before 1200 UTC the region of negative P was present. However, we have shown that radiative heating gradients associated with cirrus clouds could generate the region of negative P in situ.

This paper has presented the hypothesis that the wave disturbances observed in the satellite pictures of 25 February 1987 were excited by inertial instability. The characteristics of the cloud wavelets tend to support this hypothesis through comparison between observations and the theoretical estimates of SC. Analyses of potential vorticity fields have been used to provide further evidence of a dynamical source of the instability. The observations represent a positive verification of the theoretical and numerical prediction of asymmetric instability in SC.

One might reasonably question the relationship between these observations and the extensive work of Emanuel and collaborators (e.g., Emanuel 1979; Emanuel 1982; Nehrkorn 1986). Emanuel (1979, 1982) treated neutral waves which manifested a balance between the destabilizing influence of vertical shear and stabilizing diffusive dissipation. Perturbations with structure along the direction of the parallel jet were not considered. By contrast, the instability observed here was clearly asymmetric in structure. Nevertheless, the *effect* of the instability is similar to that assumed in Emanuel (1983b); i.e., regardless of the particular structural characteristics of the perturbations, inertial instability serves to mix the potential vorticity, causing the modified flow to have nonnegative potential vorticity.

Our ability to describe the detailed characteristics of the instability presented in this paper has been limited by the sparseness of direct observations. These deficiencies in the observational database have left us with many interesting, but unanswered questions; e.g., What is the vertical scale of the perturbed flow? Are the instabilities characterized by vertical motion? To answer these and other relevant questions requires an intensive field observational program such as FIRE Cirrus IFO (Starr 1987). An alternate, and less expensive, approach is to model these instabilities. To our knowl-

edge, explicit calculation of inertial instabilities in a two-dimensionally sheared basic state has not been accomplished. We are currently pursuing this more realistic problem using a linear spectral model.

Finally, it may be noted that initial analyses in numerical models may contain regions of negative potential vorticity and spurious rapid growth of unstable perturbations. One approach, already suggested by Dunkerton (1983) for equatorial shear, is to increase the numerical dissipation in order to eliminate the instability. Perhaps a more representative initialization procedure would include an inertial adjustment step in which fP was required to be nonnegative at every point in the domain.

Acknowledgments. The authors wish to thank Mark Ringerud, Wayne Schubert, Kerry Emanuel, and Jim Toth for their valuable comments. This work was supported by NSF Grant ATM-830579 and by the Presidential Young Investigator Award (NSF Grant ATM-8352205) to D. Stevens. Acknowledgment is made to the Cooperative Institute of Research in the Atmosphere (CIRA) for a substantial portion of the computing resources used in this research. The Department of Atmospheric Science ground station at Colorado State University collected and supplied the satellite data under the direction and support of NASA's FIRE project. The graphical displays and objective analyses were done using NASA's GEMPAK software.

APPENDIX

Basis for Comparison of Theoretical Results to Observations

We consider here the assumptions which are necessary in order to use the results of SC as a theoretical basis for the observed wave disturbances. Stevens and Ciesielski's results were obtained by using the linearized, hydrostatic equations in a horizontally sheared, zonal basic state flow on a sphere. This system of equations is separable in its vertical dependence, so that by specifying the separation constant h, SC's equations for the horizontal structure functions (u, v, Φ) were

$$\left(\frac{\partial}{\partial t} + \bar{U}\frac{\partial}{\partial z}\right)u - \bar{\eta}v + \frac{\partial \Phi}{\partial x} = 0 \quad \text{(A1)}$$

$$\left(\frac{\partial}{\partial t} + \bar{U}\frac{\partial}{\partial x}\right)v + \tilde{f}u + \frac{\partial \Phi}{\partial y} = 0 \quad \text{(A2)}$$

$$\left(\frac{\partial}{\partial t} + \bar{U}\frac{\partial}{\partial x}\right)\Phi + gh\left[\frac{\partial u}{\partial x} + \frac{\partial(v\cos\theta)}{\cos\theta\partial y}\right] = 0, \quad \text{(A3)}$$

where $dx = a\cos\theta d\phi$, $dy = ad\theta$, ϕ is longitude, θ is latitude, a is the earth's radius, (u, v, Φ) have their usual meaning and SI units; $f = 2\Omega\sin\theta$ is the Coriolis parameter,

$$\bar{\eta} = f - \frac{d(\bar{U}\cos\theta)}{\cos\theta dy}, \quad \tilde{f} = f + \frac{2\bar{U}}{a}\tan\theta$$

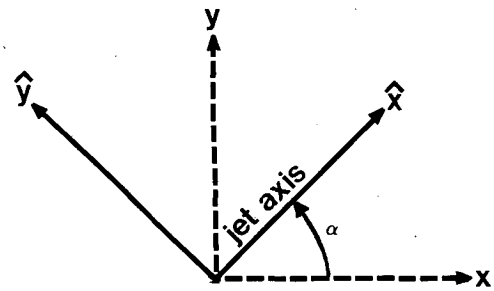

FIG. A1. The rotated coordinate system in relation to the spherical coordinate system.

are the basic state absolute vorticity and modified Coriolis parameter, respectively. A relevant parameter to this system which represents the maximum possible nondimensional growth rate for symmetric inertial instability at vanishing vertical scale is $\epsilon \equiv (-\bar{\eta}\tilde{f})^{1/2}_{\max}(2\Omega)^{-1}$.

We assume now that the spherical coordinate system is rotated counterclockwise by some angle α such that the rotated x-axis $(\hat{x})$ is aligned with the observed jet axis as shown in Fig. A1. The coordinates of these two grids are related by

$$x = \hat{x}\cos\alpha - \hat{y}\sin\alpha$$

$$y = \hat{x}\sin\alpha + \hat{y}\cos\alpha.$$

Since the observed wave disturbance, at any given instant, was confined over a narrow range of latitudes, we assume f-plane dynamics and neglect the terms in (A1)–(A3) due to the earth's sphericity. With these assumptions the equations in the rotated coordinate $(\hat{x}, \hat{y})$ have the form

$$\left(\frac{\partial}{\partial t} + \hat{U}\frac{\partial}{\partial \hat{x}}\right)\hat{u} - \hat{\eta}\hat{v} + \frac{\partial \hat{\Phi}}{\partial \hat{x}} = 0 \quad \text{(A4)}$$

$$\left(\frac{\partial}{\partial t} + \hat{U}\frac{\partial}{\partial \hat{x}}\right)\hat{v} + f\hat{u} + \frac{\partial \hat{\Phi}}{\partial \hat{y}} = 0 \quad \text{(A5)}$$

$$\left(\frac{\partial}{\partial t} + \hat{U}\frac{\partial}{\partial \hat{x}}\right)\hat{\Phi} + gh\left[\frac{\partial \hat{u}}{\partial \hat{x}} + \frac{\partial \hat{v}}{\partial \hat{y}}\right] = 0, \quad \text{(A6)}$$

where a variable in the rotated coordinates is denoted by a hat. In (A4)–(A6) the basic state quantities are averaged along $\hat{x}$, such that

$$\hat{U} = \hat{U}(\hat{y}) \quad \text{and} \quad \hat{\eta} = f - \frac{d\hat{U}}{d\hat{y}}.$$

Likewise, for this system $\hat{\epsilon} \equiv (-\hat{\eta}f)^{1/2}_{\max}(2\Omega)^{-1}$. With use of the observed data, it is now a simple matter to compute the relevant dynamical parameters. Since the assumptions which were made going from system (A1)–(A3) to (A4)–(A6) are applicable for a locally parallel jet, the theoretical results of SC should be relevant to this study.

REFERENCES

Ackerman, T. P., K. N. Liou, F. P. J. Valero and L. Pfister, 1988: Heating rates in tropical anvils. *J. Atmos. Sci.*, **45**, 1606–1623.

Arakawa, A., and V. R. Lamb, 1977: Computational design of the basic dynamical process of the UCLA general circulation model. *Methods in Computational Physics*, Vol. 17, Academic Press, 174–265.

Barnes, S. L., 1973: Mesoscale objective analysis using weighted time-series observations. *NOAA Tech. memo. ERL NSSL-62*. [Can be obtained from Environmental Research Laboratories, National Severe Storms Laboratory, Norman, Okla., 60 pp.]

Booker, J. R., and F. B. Bretherton, 1967: The critical layer for internal gravity waves in a shear flow. *J. Fluid Mech.*, **27**, 513–539.

Drazin, P. G., and L. N. Howard, 1966: Hydrodynamic stability of parallel flow of inviscid fluids. *Advances in Applied Mechanics*, Vol. 9, Academic Press, 1–89.

Dunkerton, T. J., 1983: A nonsymmetric equatorial inertial instability. *J. Atmos. Sci.*, **40**, 807–813.

Durran, D. R., and B. W. Daniel, 1988: An investigation of the poleward edges of cirrus clouds associated with midlatitude jet streams. *Mon. Wea. Rev.*, **116**, 702–714.

Emanuel, K. A., 1979: Inertial instability and mesoscale convective systems. Part I: Linear theory of inertial instability in rotating viscous fluids. *J. Atmos. Sci.*, **36**, 2425–2499.

——, 1982: Inertial instability and mesoscale convective systems. Part II: Symmetric CISK in a baroclinic flow. *J. Atmos. Sci.*, **39**, 1080–1097.

——, 1983a: On assessing local conditional symmetric instability from atmospheric soundings. *Mon. Wea. Rev.*, **111**, 2016–2033.

——, 1983b: The Lagrangian parcel dynamics of moist symmetric instability. *J. Atmos. Sci.*, **40**, 2368–2376.

Ertel, H., 1942: Ein euer hydrodynamischer Wirelsatz. *Meteor. Z.*, **59**, 271–281.

Hines, C. O., 1960: Internal gravity waves at ionospheric heights. *Can. J. Phys.*, **38**, 1441–1481.

Hoskins, B. J., 1974: The role of potential vorticity in symmetric stability and instability. *Quart. J. Roy. Meteor. Soc.*, **100**, 480–482.

Howard, L. N., 1961: Note on a paper of John W. Miles. *J. Fluid Mech.*, **10**, 509–512.

Jones, W. L., 1968: Reflection and stability of waves in stably stratified fluids with shear flow: A numerical study. *J. Fluid Mech.*, **34**, 609–624.

Kuo, H. L., 1949: Dynamic instability of two-dimensional non-divergent flow in a barotropic atmosphere. *J. Meteor.*, **6**, 105–122.

Lindzen, R. S., 1974a: Wave-CISK in the tropics. *J. Atmos. Sci.*, **31**, 156–179.

——, 1974b: Stability of a Helmholtz velocity profile in a continuously stratified, infinite Boussinesq fluid—application to clear air turbulence. *J. Atmos. Sci.*, **31**, 1507–1514.

——, and K. K. Tung, 1976: Banded convective activity and ducted gravity waves. *Mon. Wea. Rev.*, **104**, 1602–1617.

Minnis, P., and E. F. Harrison, 1984: Diurnal variability of regional cloud and clear-sky parameters derived from GOES data. Part I: Analysis method. *J. Climate Appl. Meteor.*, **23**, 993–1011.

Nehrkorn, T., 1986: Wave-CISK in a baroclinic basic state. *J. Atmos. Sci.*, **43**, 2773–2791.

Raymond, D. J., 1975: A model for predicting the movement of continuously propagating convective storms. *J. Atmos. Sci.*, **32**, 1308–1317.

Shapiro, M. A., 1981: Frontogenesis and geostrophically forced secondary circulations in the vicinity of jet stream-frontal zone systems. *J. Atmos. Sci.*, **38**, 954–973.

Smith, R. B., 1979: The influence of mountains on the atmosphere. *Advance in Geophysics*, **21**, Academic Press, 87–228.

Starr, D. O'C., 1987: A cirrus-cloud experiment: Intensive field observations planned for FIRE. *Bull. Amer. Meteor. Soc.*, **68**, 119–124.

——, and S. K. Cox, 1985: Cirrus Clouds. Part I: A cirrus cloud model. *J. Atmos. Sci.*, **42**, 2663–2681.

Stevens, D. E., 1983: On symmetric stability and instability of zonal mean flows near the equator. *J. Atmos. Sci.*, **40**, 882–893.

——, and P. E. Ciesielski, 1986: Inertial instability of horizontally sheared flow away from the equator. *J. Atmos. Sci.*, **43**, 2845–2856.

——, and F. X. Crum, 1987: Dynamic Meteorology. *The Encyclopedia of Physical Science and Technology*, Academic Press, 227–260.

Weldon, R. B., 1979: Cloud patterns and upper air wind field. *Part IV, Satellite Training Course Notes*. [Can be obtained from Satellite Application Laboratory, NES-DIS/NOAA, Washington, DC, 20233, 80 pp.]